



Three-dimensional MHD simulation of CMEs in three-dimensional background solar wind with the self-consistent structure on the source surface as input: Numerical simulation of the January 1997 Sun-Earth connection event

Fang Shen,¹ Xueshang Feng,¹ S. T. Wu,² and Changqing Xiang¹

Received 4 November 2006; revised 26 February 2007; accepted 13 March 2007; published 12 June 2007.

[1] A three-dimensional time-dependent, numerical magnetohydrodynamic (MHD) model is used to investigate the propagation of coronal mass ejections (CMEs) in the nonhomogenous background solar wind flow. On the basis of the observations of the solar magnetic field and K-coronal brightness, the self-consistent structure on the source surface of 2.5 Rs is established with the help of MHD equations. Using the self-consistent source surface structures as initial-boundary conditions, we develop a three-dimensional MHD regional combination numerical model code to obtain the background solar wind from the source surface of 2.5 Rs to the Earth's orbit (215 Rs) and beyond. This model considers solar rotation and volumetric heating. Time-dependent variations of the pressure and velocity configured from a CME model at the inner boundary are applied to generate transient structures. The dynamical interaction of a CME with the background solar wind flow between 2.5 and 215 Rs (1 AU) is then investigated. We have chosen the well-defined halo-CME event of 6–12 January 1997 as a test case. Because detailed observations of this disturbance at 1 AU (by WIND spacecraft) are available, this event gives us an excellent opportunity to verify our MHD methodology and to learn about the physical processes of the Sun-Earth connection. In this study, we find that this three-dimensional MHD model, with the self-consistent structures on the source surface as input, provides a relatively satisfactory comparison with the WIND spacecraft observations.

Citation: Shen, F., X. Feng, S. T. Wu, and C. Xiang (2007), Three-dimensional MHD simulation of CMEs in three-dimensional background solar wind with the self-consistent structure on the source surface as input: Numerical simulation of the January 1997 Sun-Earth connection event, *J. Geophys. Res.*, *112*, A06109, doi:10.1029/2006JA012164.

1. Introduction

[2] Space weather research is of growing importance to the scientific community and can affect human activities. Interplanetary coronal mass ejections (ICMEs, including their shocks) and vast structures of plasma and magnetic fields that are expelled from the Sun outward through the heliosphere are now known to be a key causal link between solar eruptions and major interplanetary and geomagnetic disturbances [Dryer, 1994]. In order to realistically reflect the properties of three-dimensional CME propagation, the numerical research of three-dimensional background solar wind has become one of key problems that have to be solved for modeling space weather events.

[3] CMEs and their interplanetary consequences (ICMEs) represent different aspects of the same phenomenon responsible for large geomagnetic storms [Gosling, 1990]. Because of the great complexity, each aspect has typically been investigated separately. This approach is useful for revealing the basic underlying physics; however, a complete picture requires a comprehensive model of all of the processes considered together. Successful merging of two-dimensional and three-dimensional magnetohydrodynamic (MHD) coronal and heliospheric models has been reviewed and performed by Dryer [1974, 1975, 1982, 1994], Dryer [1998], Usmanov and Dryer [1995], Wu *et al.* [1997, 1999], Odstrcil *et al.* [2002a, 2004a], and Manchester *et al.* [2005]. The coronal simulation conducted by Odstrcil *et al.* [2002a] started from an initial potential magnetic field and spherically symmetric Parker solar wind. The plasma density and the temperature at the boundary were given as constants, and the radial velocity was determined at each time step by solving the gas characteristic equations. In the work by Odstrcil *et al.* [2002b], the coronal model, whose domain extends from the photosphere up to 30 Rs, was based on the three-dimensional resistive MHD equations that were

¹SIGMA Weather Group, State Key Laboratory for Space Weather, Center for Space Science and Applied Research, Chinese Academy of Sciences, Beijing, China.

²Center for Space Plasma and Aeronomic Research, The University of Alabama in Huntsville, Huntsville, Alabama, USA.

solved by a semi-implicit finite difference scheme using staggered values, while the heliospheric model, whose domain extends from 30 to 275 Rs, was based on the three-dimensional ideal MHD equations that were solved by an explicit finite difference Total Variation Diminishing/Lax-Friedrichs (TVD/LF) scheme using cell-centered values. The output from the coronal model consisted of a temporal sequence of MHD flow parameters, which were used as a boundary condition for the heliospheric model. An alternative procedure that included a three-dimensional kinematic approach for shock arrival prediction procedures was described by *Fry et al.* [2001, 2003].

[4] *Usmanov et al.* [2000] also used a global axisymmetric MHD solar wind model with WKB Alfvén waves, which were simulated by combining a time relaxation numerical technique in the two-dimensional solar corona region (1–22 Rs) with a marching-along-radius method in the outer region (22 Rs–10 AU). In the coronal region, they assumed the initial state of the magnetic field as a dipole, and the hydrodynamic variables were given by a Parker-type solution of the one-dimensional HD equations [*Parker, 1963*]. Once a steady state solution in the inner region was obtained, a slice of the solution at the interface between the two regions interface (22 Rs) was used as the inner boundary condition to start integration throughout the outer region [*Usmanov, 1993; Usmanov and Dryer, 1995; Usmanov et al., 2000*]. Their global steady state axisymmetric MHD model successfully reproduced quantitatively the observations made by *Ulysses* during its first fast latitude traversal in 1994–1995 [*Usmanov and Dryer, 1995; Usmanov et al., 2000*].

[5] The large-scale structure of solar wind observed by *Ulysses* near solar minimum was also simulated by *Feng et al.* [2005] by using the three-dimensional numerical MHD model. Their model combined the TVD Lax-Friedrich scheme and MacCormack II scheme and divided the computational domain into two regions as follows: one from 1 to 22 Rs and the other from 18 Rs to 1 AU. On the basis of the observations of the solar photospheric magnetic field and an addition of the volumetric heating [*Suess et al., 1996; Wang et al., 1998*] to MHD equations, the large-scale bimodal solar wind (i.e., fast and slow wind) structure mentioned above was reproduced by using the three-dimensional MHD model, and their numerical results were roughly consistent with *Ulysses*' observations. Their simulation showed that the initial magnetic field topology and the addition of volume heating could govern the bimodal structure of solar wind observed by *Ulysses* and also demonstrated that the three-dimensional MHD numerical model used by them was efficient in modeling the large-scale solar wind structure.

[6] *Riley et al.* [2001; see also *Linker et al., 1999*] proposed an empirically driven global MHD model of the solar corona and inner heliosphere. They used the output of the coronal solution directly to provide the inner boundary condition of the heliospheric model. In modeling the solar corona they specified at the lower boundary the radial component of the magnetic field B_r based on the observed line-of-sight measurements of the photospheric magnetic field. Uniform characteristic values were used for the plasma density and temperature. Initial estimates of the field and plasma parameters were found from a potential field model

and a Parker transonic solar wind solution [*Parker, 1963*], respectively. Their results showed that the simulations reproduced the overall large-scale features of the observations during the “whole Sun month” (August/September 1996), although the specified lower boundary conditions were very approximate.

[7] The self-consistent, time-dependent initial and boundary conditions with solar rotation, on the basis of observation results, will play a very important role in three-dimensional background solar wind numerical model, and the work devoted to this aspect is still at its initial stage. In this paper, on the basis of the observation of the solar magnetic field and K-coronal brightness, the self-consistent structures on the source surface are established with the help of MHD equations at 2.5 Rs according to the global distribution of coronal mass output's flux F_m (density $\rho \times$ speed v) by *Wei et al.* [2003]. By using the self-consistent source surface structures as initial and boundary conditions, we have successfully developed a three-dimensional magnetohydrodynamic (MHD) regional combination numerical model [*Feng et al., 2005*] of background solar wind, from the source surface of 2.5 Rs to near the Earth's orbit (215 Rs) and beyond. This model includes solar rotation and volumetric heating. Once a steady state solar wind is produced, we use a CME model as input into the inner boundary of 2.5 Rs. The dynamical interaction of a CME with the background solar wind flow between 2.5 and 215 Rs (1 AU) is investigated. Observations of the 6–12 January 1997 Sun–Earth connection event are used as a test for our numerical simulation. A brief description of the observations is given in section 2. The three-dimensional MHD regional combination numerical model of background solar wind, which includes self-consistent initial and boundary conditions, is described in section 3. The three-dimensional numerical simulation of CMEs is given in section 4. Numerical results and comparisons with the observations are presented in section 5. Finally, the concluding remarks are given in section 6.

2. Observation of the 6–12 January 1997 Halo-CME

[8] Many CMEs observed near the solar limb maintain angular widths that are nearly constant as a function of height [*Webb et al., 1997*] and propagate almost radially beyond the first few solar radii [*Plunkett et al., 1997*]. On the basis of these properties of limb CMEs, the empirical cone descriptive assumption for halo-CMEs was developed by *Zhao et al.* [2002] with free parameters that characterize the angular width of the cone and the orientation of the central axis of the cone. The free parameters can be determined by matching the cross section of the cone at a specified radial distance projected on the sky plane with the observed bright ring of the halo-CME at a specified time. The cone model was also used in the numerical simulation by *Odstrcil et al.* [2004b, 2005]. The reader is reminded that the approach of *Zhao et al.* [2002] is an empirical one, whereas the present model is a physics-based three-dimensional MHD one that starts “cone-like” but expands because of the anisotropic wave dynamics.

[9] Detailed descriptions of the 6–12 January 1997 event have been reported by a number of authors [Burlaga *et al.*, 1998; Webb *et al.*, 1998; Fox *et al.*, 1998; Wu *et al.*, 1999, 2002; Michalek *et al.*, 2003; Cane and Richardson, 2003]. For completeness we will summarize some of the highlights in this section.

[10] The CME was observed first in the C2 coronagraph on 6 January 1997 at 17:34 UT and later in the C3 coronagraph before 19:50 UT [Webb *et al.*, 1998] and appeared as a partial arc moving at $\sim 20^\circ\text{S}$ and $\sim 3^\circ\text{W}$ of the central meridian [Michalek *et al.*, 2003]. These observations were followed on 10 and 11 January 1997 by a well-observed magnetic cloud that passed the WIND spacecraft located in the solar wind upstream of Earth [Burlaga *et al.*, 1998]. According to Webb *et al.* [1998], it was halo-like and the traveltime to Earth was about 85 hours which was right for a CME with a typical speed of 450 km/s. It had a large angular span bigger than 140° , greatly exceeding those of most CMEs. Measurements of the expansion speed of the front by a height/time diagram yield a speed of about 100–150 km/s [Wu *et al.*, 2002]. As reported by Wu *et al.* [1999] the source of this CME event is related to the disappearance of a filament located at $\sim 20^\circ\text{S}$ and $\sim 4^\circ\text{W}$ of the central meridian according to ground-based $H\text{-}\alpha$ observation.

[11] The central axis of the CME model pointed to 20°S , 03°W while its half angular width is about 52.5° [Michalek *et al.*, 2003]. We assume that the leading edge of the CME reached a radial height of 2.5 Rs with a speed of 160 km/s. This speed is almost consistent with the projection-corrected speed by using SOHO observations and the formula derived by Hundhausen *et al.* [1994].

3. Background Solar Wind

3.1. Computational Mesh

[12] To obtain the proper spatial and temporal resolutions, the computational domain is divided into two regions as follows: $2.5 \text{ Rs} \leq r \leq 22 \text{ Rs}$ (region I) and $18 \text{ Rs} \leq r \leq 215 \text{ Rs}$ (region II) (radial direction), $-75^\circ \leq \theta \leq 75^\circ$ (meridional direction, both regions), and $0^\circ \leq \varphi \leq 360^\circ$ (azimuthal direction, both regions). The direction $\varphi = 180^\circ$, $\theta = 0^\circ$ corresponds to the Earth's position shown in Figure 1.

[13] The grid network for region I is chosen to be $84(r) \times 55(\theta) \times 90(\varphi)$. The grid size is uniform in azimuth, with $\Delta\varphi = 4^\circ$. The radial grid (r_i) and meridional grid (θ_j) are not uniform. In order to obtain proper computational resolution, we choose for the radial grid as follows: $r(1) =$

2.5 Rs , $\Delta r(1) = \text{step} \times r(1)$, $r(i) = r(i-1) + \Delta r(i-1)$, $\Delta r(i) = \text{step} \times r(i-1)$, $\text{step} = \pi/54$ ($\pi = 3.1415926$). For the meridional grid we choose $\Delta\theta(0^\circ) = 1.0^\circ$, $\Delta\theta(-75^\circ) = \Delta\theta(75^\circ) = 5.0^\circ$, with a constant increase in $\Delta\theta$ from $\theta = 0^\circ$ to $\theta = \pm 75^\circ$.

[14] The grid network of θ and φ for region II is the same as that for region I, but with $\Delta r = 0.075 \text{ Rs}$. In fact, the radial coordinate r can be treated as a time-like coordinate, and a three-dimensional steady MHD flow can be solved by a two-dimensional (θ and φ), “time” (r)-dependent formulation, which is prescribed in detail in section 3.4.

3.2. Region I (2.5~22 Rs)

3.2.1. Physical Modeling

[15] In the transonic, trans-Alfvénic inner region, three-dimensional ideal MHD equations, which include solar rotation to generate spiral configuration of the magnetic field in the heliosphere and volumetric heating to produce bimodal solar wind structure seen by Ulysses, are used to describe the dynamic behavior of the coronal and solar wind plasma for this study. Conventionally, it is advantageous to solve the equations in the inertial (nonrotating) reference frame because of the computational difficulties associated with the monotonic growth of the azimuthal component of the velocity v_φ at large radii [Pizzo, 1982]. Transformation from the rotating frame is affected by substituting

$$\vec{v} = \vec{u} - \Omega r \sin\theta \vec{\varphi} \quad (1)$$

where (r, θ, φ) denotes the spherical coordinate system with its origin at the Sun's center. The velocity \vec{u} and \vec{v} denote, respectively, the velocities in the inertial frame and in the reference frame rotating with the Sun. Ω is the angular velocity of the Sun. Equation (1) can be rewritten as

$$v_r = u_r, \quad v_\theta = u_\theta, \quad v_\varphi = u_\varphi - \Omega r \sin\theta \quad (2)$$

[16] These inertial frame equations can be written in a spherical-component form as follows:

$$\frac{\partial U}{\partial t} + \frac{1}{r^2} \frac{\partial r^2 F}{\partial r} + \frac{1}{r \sin\theta} \frac{\partial \sin\theta G}{\partial \theta} + \frac{1}{r \sin\theta} \frac{\partial H}{\partial \varphi} = S \quad (3)$$

where

$$U = \begin{pmatrix} \rho \\ \rho u_r \\ \rho u_\theta \\ \rho v_\varphi \\ B_r \\ B_\theta \\ B_\varphi \\ p \end{pmatrix}, F = \begin{pmatrix} \rho u_r \\ \rho u_r^2 \\ \rho u_r u_\theta \\ \rho u_r v_\varphi \\ 0 \\ u_r B_\theta - u_\theta B_r \\ u_r B_\varphi - v_\varphi B_r \\ \rho u_r \end{pmatrix}, G = \begin{pmatrix} \rho u_\theta \\ \rho u_r u_\theta \\ \rho u_\theta^2 \\ \rho u_\theta v_\varphi \\ u_\theta B_r - u_r B_\theta \\ 0 \\ u_\theta B_\varphi - v_\varphi B_\theta \\ \rho u_\theta \end{pmatrix}, H = \begin{pmatrix} \rho v_\varphi \\ \rho u_r v_\varphi \\ \rho u_\theta v_\varphi \\ \rho v_\varphi^2 \\ v_\varphi B_r - u_r B_\varphi \\ v_\varphi B_\theta - u_\theta B_\varphi \\ 0 \\ \rho v_\varphi \end{pmatrix}$$

$$S = \begin{pmatrix} 0 \\ -\frac{1}{r^2} \frac{\partial}{\partial r} \left(r^2 \left(p + \frac{B^2}{2\mu_0} - \frac{B_r^2}{\mu_0} \right) \right) + \frac{1}{r \sin \theta} \frac{\partial}{\partial \theta} \left(\frac{\sin \theta B_r B_\theta}{\mu_0} \right) + \frac{1}{r \sin \theta} \frac{\partial}{\partial \varphi} \left(\frac{B_r B_\varphi}{\mu_0} \right) \\ + \frac{2p}{r} + \rho \frac{u_\theta^2 + v_\varphi^2}{r} + \frac{B_r^2}{r\mu_0} - \frac{\rho G M_s}{r^2} + f_r \\ \frac{1}{r^2} \frac{\partial}{\partial r} \left(\frac{r^2 B_r B_\theta}{\mu_0} \right) - \frac{1}{r \sin \theta} \frac{\partial}{\partial \theta} \left(\sin \theta \left(p + \frac{B^2}{2\mu_0} - \frac{B_\theta^2}{\mu_0} \right) \right) + \frac{1}{r \sin \theta} \frac{\partial}{\partial \varphi} \left(\frac{B_\theta B_\varphi}{\mu_0} \right) \\ + \frac{\cot \theta}{r} \left(p + \frac{B^2}{2\mu_0} \right) + \rho \frac{v_\varphi^2 \cot \theta - u_r v_\theta}{r} - \frac{B_\varphi^2 \cot \theta - B_r B_\theta}{r\mu_0} + f_\theta \\ \frac{1}{r^2} \frac{\partial}{\partial r} \left(\frac{r^2 B_r B_\varphi}{\mu_0} \right) + \frac{1}{r \sin \theta} \frac{\partial}{\partial \theta} \left(\frac{\sin \theta B_\varphi B_\theta}{\mu_0} \right) - \frac{1}{r \sin \theta} \frac{\partial}{\partial \varphi} \left(\sin \theta \left(p + \frac{B^2}{2\mu_0} - \frac{B_\varphi^2}{\mu_0} \right) \right) \\ - \rho \frac{u_r v_\varphi + u_\theta v_\varphi \cot \theta}{r} + \frac{B_r B_\varphi + B_\theta B_\varphi \cot \theta}{r\mu_0} + f_\varphi \\ 0 \\ (B_\theta u_r - B_r u_\theta)/r \\ (u_\theta B_\varphi - v_\varphi B_\theta) \cot \theta + (v_r B_\varphi - v_\varphi B_r)/r \\ -(\gamma - 1)p \nabla \cdot \vec{v} + (\gamma - 1)Q \end{pmatrix} \quad (4)$$

with

$$p = \rho RT \quad (5)$$

$$\begin{aligned} f_r &= \rho \Omega \sin \theta (2\nu_\varphi + \Omega r \sin \theta) \\ f_\theta &= \rho \Omega \cos \theta (2\nu_\varphi + \Omega r \sin \theta) \\ f_\varphi &= -\rho \Omega \left((4u_r \sin \theta + 3\nu_\theta \cos \theta) \right. \\ &\quad \left. + \left(r \sin \theta \frac{\partial u_r}{\partial r} + \sin \theta \frac{\partial u_\theta}{\partial \theta} + \frac{\partial v_\varphi}{\partial \varphi} \right) \right) \end{aligned} \quad (6)$$

where ρ is the bulk plasma density, T is the bulk plasma temperature, $B = (B_r, B_\theta, B_\varphi)$ is the magnetic field, μ_0 is the magnetic permeability, R is the gas constant ($1.653 \times 10^{-2} \text{ km}^2 \text{ s}^{-2} \text{ K}^{-1}$), γ is the specific heat ratio, M_s is the solar mass, G is the gravity constant. f_r, f_θ, f_φ are inertial centrifugal forces in the r, θ, φ directions; Q is the volumetric heating function. The latter is used to parameterize the effects of coronal heating processes, heat, and radiation transfer effects [Groth *et al.*, 2000]. As the physical understanding of coronal heating processes remains limited, there is some freedom in choosing this source function. A function that includes both local energy deposition and losses is adopted herein. Furthermore, the heat source is taken to decrease exponentially [Wang *et al.*, 1998] with radial distance from the Sun. Specially, the volumetric heating function Q is assumed to have the form

$$Q = -\rho q_0 (T - T_0) \exp \left[-\frac{(r - R_s)^2}{\sigma_0^2} \right] \quad (7)$$

where T_0 and q_0 have the same meaning with that in the work of Groth *et al.* [2000]. $T_0(\theta = 0^\circ) = 1.5 \times 10^6 \text{ K}$, $T_0(\theta = \pm 75^\circ) = 2.6 \times 10^6 \text{ K}$, $\sigma_0 = 4.5 R_s$.

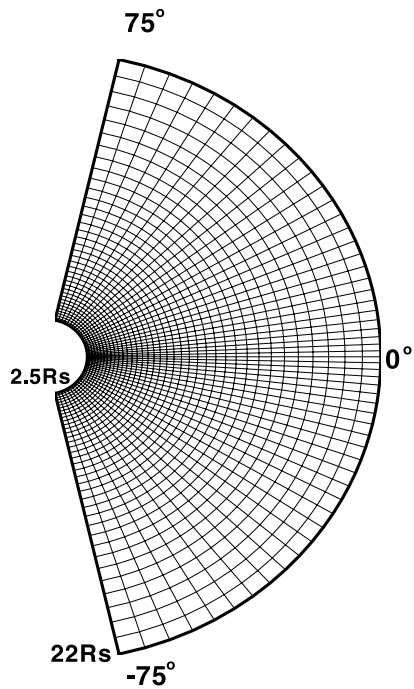
3.2.2. Self-Consistent Initial-Boundary Conditions

[17] In recent years, because of the development of the interplanetary scintillation (IPS) technique [Wei and Dryer, 1991; Manoharan *et al.*, 1995; Janardhan *et al.*, 1996; Asai *et al.*,

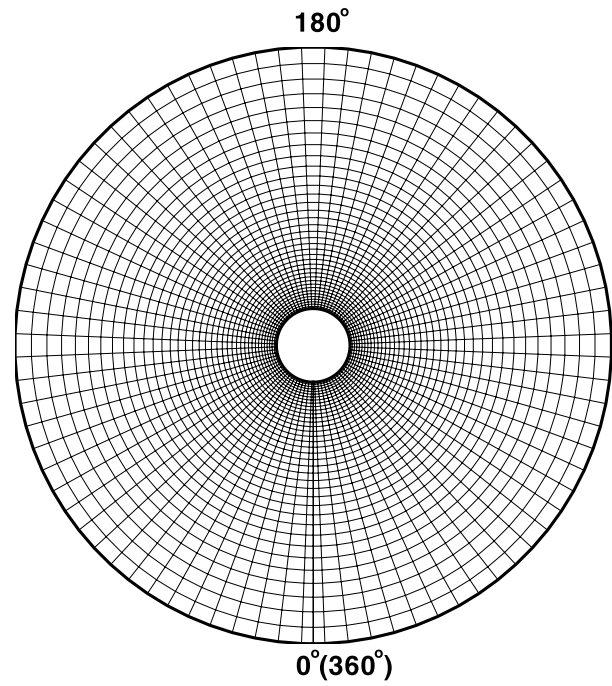
1998; Jackson *et al.*, 1998] and the improvement of observation and computational methods of the photospheric magnetic fields and the K-coronal brightness [Hoeksema, 1992; Zhao and Hoeksema, 1996; Wei *et al.*, 2003; Rickett and Coles, 1991], one can obtain large-scale structures of solar wind plasma and their evolution with various solar activities and study the relationship among the coronal density, solar wind speed, and magnetic field [Kojima *et al.*, 2001; Wei and Dryer, 1991; Wei *et al.*, 2003].

[18] Wei *et al.* [2003] analyzed the global distribution of coronal mass output's flux F_m (density $\rho \times$ speed v) at 2.5 Rs and its relation to solar magnetic field structures by using observational data from K-coronal brightness, photospheric magnetic field, and interplanetary scintillation. We need these parameters to close our equations, thus we start from 2.5 Rs instead of 1 Rs. If we can obtain such a mass flux distribution at 1 Rs, we will be able to begin from 1 Rs.

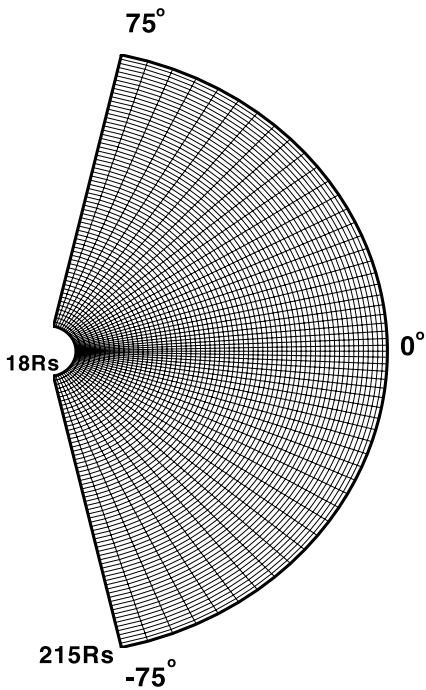
[19] Using the observational data from K-coronal brightness and photospheric magnetic field for Carrington rotation (CR) 1917–1918, the distribution of density and magnetic field can be deduced from 2.5 to 22 Rs. Figure 2 shows the distribution of the radial magnetic field and proton number density at 2.5 Rs from the observation for CR 1917–1918 at the source surface (2.5 Rs). Then, a numerical study of the global distributions at 2.5 Rs for the CR 1917–1918 was made by solving a self-consistent MHD system based on the observational data of K-coronal brightness and the photospheric magnetic fields [Wei *et al.*, 2003]. The ideal MHD equations are used for a qualitative study of F_m on the source surface in which the assumption of the radial flow and magnetic field on the source surface at 2.5 Rs is adopted as many authors used to do in making data analyses and numerical studies [e.g., Wang and Sheeley, 1990; Riley *et al.*, 1997; Smith, 2001; Liewer *et al.*, 2001; Wei *et al.*, 2003; Fry *et al.*, 2003, 2005; Detman *et al.*, 2006; McKenna-Lawlor *et al.*, 2006]. The equations consist of the six MHD equations plus the additional equations specifying pressure equilibrium



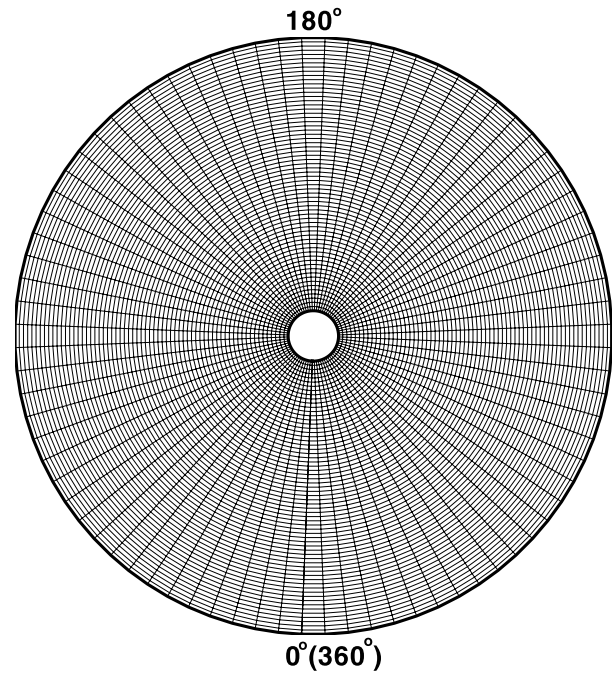
(a1) Meridional plane of Coronal Model



(a2) Equatorial plane of Coronal Model-Region I



(b1) Meridional plane of Heliospheric Model



(b2) Equatorial plane of Heliospheric Model-Region II

Figure 1. Merged numerical grids at $r - \theta$ plane and $r - \varphi$ plane of the coronal model (a1 and a2) and heliospheric model (b1 and b2).

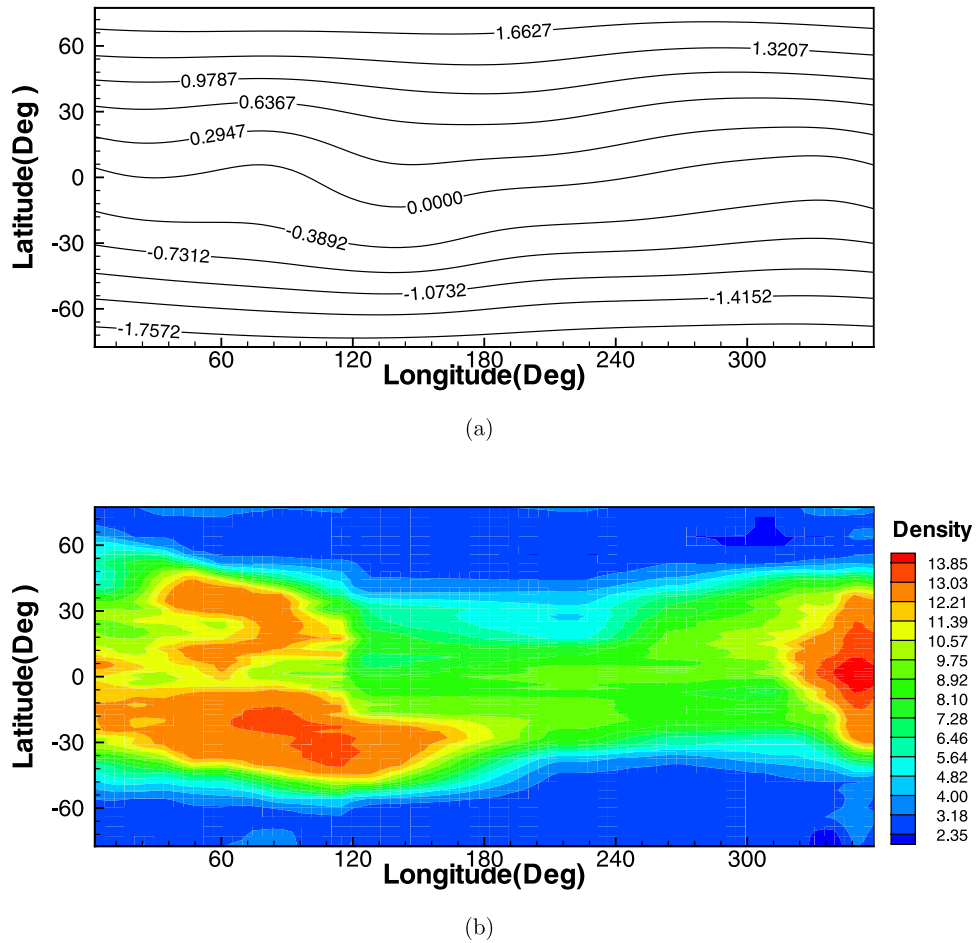


Figure 2. (a) Distribution of the radial magnetic field (10^4 nT) and (b) proton number density (10^5 cm $^{-3}$) at 2.5 Rs from observation for CR 1917-1918.

under the assumption of the radial flow and that of the statistic result for F_m . There are 10 parameters in the eight governing equations. In the case investigated, the radial magnetic field and density are two known inputs on the source surface at 2.5 Rs, thus the equations can be solved for the other eight unknown parameters [Wei *et al.*, 2003].

[20] The initial conditions of density (ρ) and magnetic field (B_r , B_θ , B_ϕ) from 2.5–22 Rs can be deduced from the observation of K-coronal brightness and photospheric magnetic field for CR 1917–1918 according to an observation-based model of solar wind background [Xiang and Feng, 2006]. On the basis of the self-consistent boundary conditions at 2.5 Rs, the initial radial distribution of $v_r(r, \theta, \varphi)$ can be found from the conservation of mass flux:

$$(\nu_r(r, \theta, \varphi)r^2\rho(r, \theta, \varphi))|_{r=2.5R_s} = (\nu_r(r, \theta, \varphi)r^2\rho(r, \theta, \varphi))|_{2.5R_s < r < 22R_s}$$

Then, ignoring the electric field in the initial state, the magnetic field and flow are rigorously aligned in the rotating frame [Pizzo, 1982]. Accordingly, $v_\theta = v_r \frac{B_\theta}{B_r}$, $v_\phi = v_r \frac{B_\phi}{B_r}$. The temperatures are mapped from the source surface (2.5 Rs) to any position between 2.5 and 22 Rs by a simple empirical radial relation of solar wind temperature, $T(r, \theta, \varphi) \propto r^{-1.25}$ [Wei *et al.*, 2003].

[21] At the outer boundary of 22 Rs, linear extrapolations are used to specify the plasma parameters.

3.3. Region II (18~215 Rs)

3.3.1. Physical Modeling

[22] Region II is a supersonic and super-Alfvénic region. Here the nonconservative inertial frame form of the steady state three-dimensional MHD equations in spherical coordinates can be written as follows:

$$A \frac{\partial U}{\partial r} + B \frac{\partial U}{\partial \theta} + C \frac{\partial U}{\partial \phi} = S + S' \quad (8)$$

where $U = (\rho, u_r, u_\theta, \nu_\phi, p, B_r, B_\theta, B_\phi)^T$, A , B , and C are 8×8 matrices, and S is a vector containing eight components which were all given by Han *et al.* [1988]. One must also pay attention to the fact that the fifth component is replaced by the divergence-free condition of the magnetic field [Han *et al.*, 1988], i.e.,

$$\frac{\partial B_r}{\partial r} + \frac{1}{r} \frac{\partial B_\theta}{\partial \theta} + \frac{1}{r \sin \theta} \frac{\partial B_\phi}{\partial \phi} = -\frac{2B_r}{r} - \frac{\text{ctg} \theta}{r} B_\theta \quad (9)$$

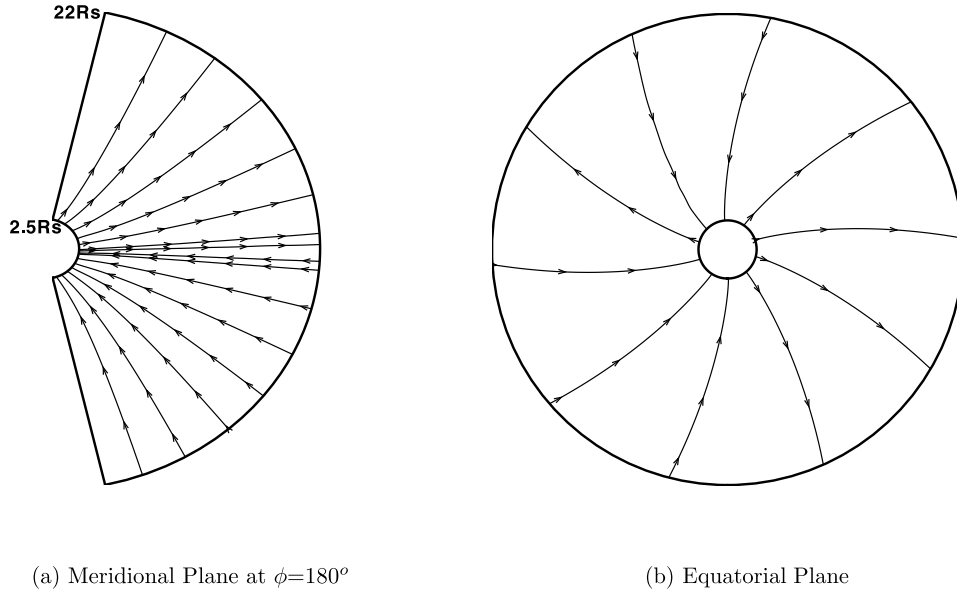


Figure 3. The calculated steady state solution for magnetic field in region I at 80 hours.

S' is the vector related with solar rotation:

$$S' = \begin{pmatrix} 0 \\ \rho\Omega \sin \theta (2\nu_\phi + \Omega r \sin \theta) \\ \rho\Omega \cos \theta (2\nu_\phi + \Omega r \sin \theta) \\ -2\Omega(u_r \sin \theta + u_\theta \cos \theta) \\ 0 \\ 0 \\ 0 \\ 0 \\ 0 \\ 0 \end{pmatrix} \quad (10)$$

where Ω and the relationship between (u_r, u_θ, u_ϕ) and (v_r, v_θ, v_ϕ) are given by equations (1) and (2).

3.3.2. Boundary Condition

[23] The inner boundary parameters are given by the coronal solution at 18 Rs from the region I model.

3.4. Three-Dimensional MHD Regional Combinational Numerical Simulation

[24] The coronal model of region I, described in section 3.2.1 and on the basis of the time-dependent three-dimensional ideal MHD equations, is solved by a modified Total Variation Diminishing/Lax-Friedrichs (TVD/LF) scheme [Feng *et al.*, 2003a, 2003b, 2005] with the electric field modification method [Tóth, 2000]. This numerical model satisfies $\nabla \cdot \vec{B} = 0$ to round-off error. This is achieved by the field-interpolated central difference approach for solving the magnetic field [Tóth, 2000] in the coronal model.

[25] For the supersonic and super-Alfvénic MHD flow in the heliospheric model of region II, which expands along the radial direction, the flow conditions at a given radial position are not influenced by the downstream flow conditions. In this respect, the radial coordinate can be treated as a time-like coordinate, and a three-dimensional steady MHD flow can be solved by a two-dimensional (θ and ϕ),

“time” (r)-dependent formulation. We treat the radial coordinate as a time-like coordinate and apply the MacCormack II scheme as done by Feng *et al.* [2005] to equation (8). The numerical stability requirements dictate the size of radial increment Δr at each marching step. The usual Courant-Friedrichs-Levy (CFL) condition is used to determine the maximum permissible increment:

$$\Delta r \leq \min \left(\frac{\Delta \theta}{\max |\xi|}, \frac{\Delta \phi}{\max |\zeta|} \right) \quad (11)$$

where ξ and ζ are the characteristic speeds along the meridional and azimuthal directions [Han *et al.*, 1988; Feng *et al.*, 2005].

[26] The ratio of specific heats is given as $\gamma = 1.05$ at the coronal model of region I and $\gamma = 1.2$ at the heliospheric model of region II.

3.5. Numerical Result of Background Solar Wind

[27] Figures 3 and 4 show the calculated steady state magnetic field topology in the meridional plane at $\phi = 180^\circ$ (left) and equatorial plane (right) in the corona and heliosphere at 80 hours, respectively. The famous Archimedes’ spiral lines appear in the right panels of Figures 3 and 4.

[28] Figure 5 shows the ambient state in the corona at 80 hours after the time-dependent solution is obtained, using the well-known relaxation procedure, prior to imposition of the pulses that are described in section 4. Profiles of the radial magnetic field, proton number density, temperature, and the radial velocity at $\theta = 10^\circ$ (radial profiles) and $r = 18$ Rs (meridional profiles at $\phi = 180^\circ$) are shown in the left and right panels, respectively.

[29] The heliospheric simulation of the solar wind is driven by flow parameters of the solar corona at 18 Rs. Figure 6 shows the ambient state in the heliosphere at 80 hours. Profiles of the radial magnetic field, proton number density, temperature, and the radial velocity at $\theta = 10^\circ$ (radial profiles) and $r = 215$ Rs (meridional profiles at $\phi = 180^\circ$) are shown in the left and right panels, respectively.

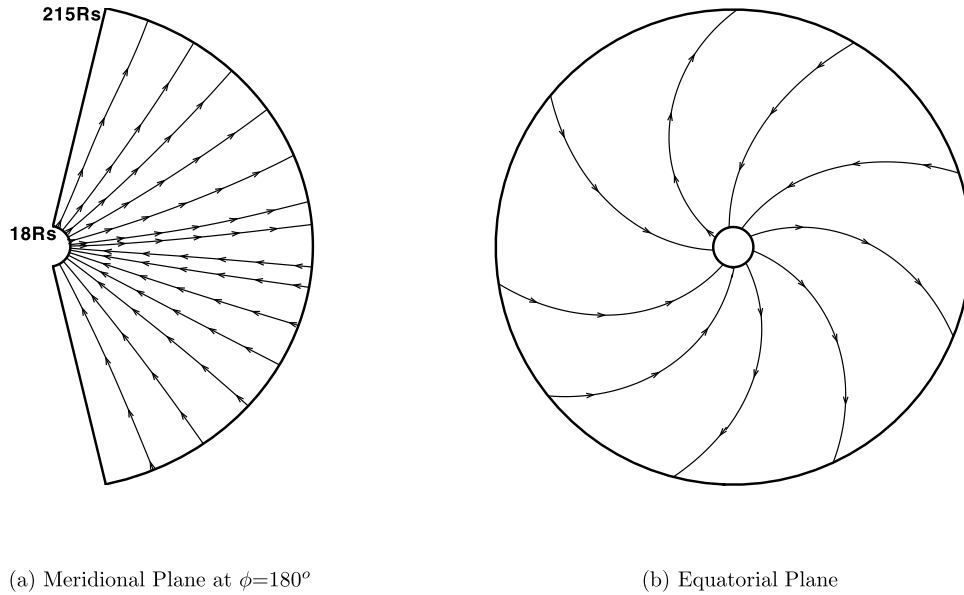


Figure 4. The calculated steady state solution for magnetic field in region II at 80 hours.

Both the configurations of corona and heliosphere consist of a dense and slow flow near the current sheet. The range of latitude is about $\pm 25^\circ$. The absolute value of the radial magnetic field almost remains constant, independent with latitude, which is consistent with the Ulysses observation.

[30] Figure 7 shows the combined radial plasma parameter profiles for regions I and II at $\theta = 10^\circ$ and $\varphi = 180^\circ$. The density, radial velocity, and radial magnetic field show smooth transitions between coronal and heliospheric models corresponding to the expanding plasma. The temperature has a sharp change in the slope of its radial profile that is caused by the jump in the ratio of specific heats between coronal and heliospheric models ($\gamma = 1.05$ and 1.2, respectively).

4. Numerical Simulation of CMEs Propagation

[31] The CME is introduced near the inner boundary of 2.5 Rs at the location where the disappearance of a filament occurred (i.e., $\sim 20^\circ\text{S}$ and 3°W) as a time-dependent pulse. This pulse consists of pressure and momentum pulses to simulate the effects of the disappearance of a filament, as done for mimicking flare input by *Han et al.* [1988], *Smith and Dryer* [1990], *Odstrcil et al.* [1996a, 1996b], *Odstrcil and Pizzo* [1999], and *Groth et al.* [2000] in the two-dimensional and three-dimensional MHD context. Up to now, the approximate solar observations to use for “mimicking” solar flare/filament and CME imitation are challenging problems.

[32] Once a steady state solar wind is obtained, we input a filament disappearance-induced CME into the inner boundary. We model a CME as follows:

$$\begin{cases} \nu_{\text{CME}}(t, \xi) = V_{\text{max}}A(\xi)B(t) \\ \rho_{\text{CME}}(t, \xi) = \rho_{\text{max}}A(\xi)B(t) \\ T_{\text{CME}}(t, \xi) = T_{\text{max}}A(\xi)B(t). \end{cases} \quad (12)$$

where

$$A(\xi) = \cos\left(\frac{\pi\xi}{2\xi_0}\right), \quad 0 \leq \xi \leq \xi_0 \quad (13)$$

$$B(t) = \begin{cases} \frac{t}{\tau_1} & (0 \leq t < \tau_1) \\ 1 & (\tau_1 \leq t < \tau_1 + \tau_m) \\ \frac{\tau_1 + \tau_m + \tau_2 - t}{\tau_2} & (\tau_1 + \tau_m \leq t \leq \tau_1 + \tau_m + \tau_2). \end{cases} \quad (14)$$

[33] Here ξ and ξ_0 are, respectively, the angles relative to the central axis of the CME and the initial angular width radius of the CME (here $\xi_0 = 52.5^\circ$). The axis of the initial simulated CME is at 20°S , 03°W (i.e., $\theta = -20^\circ$, $\varphi = 183^\circ$) to conform to the location of the filament disappearance (see section 2). Also, $t = 0$ hour in the simulation is taken to be at 17:34 UT on 6 January 1997, when the CME is first observed in the C2 coronagraph of SOHO/LASCO. τ_1 and τ_2 are, respectively, the ramp-up and ramp-down times (linear transition between the background and constant perturbation values), and τ_m is the duration of the perturbation at maximum value. This form of input-perturbation enhances a spherical wedge of solar surface since it has no latitudinal dependence. V_{max} , ρ_{max} , and T_{max} represent, respectively, the amplitude of the perturbation of the radial velocity, density, and temperature.

[34] This perturbation will be started by the following relation:

$$\begin{cases} \nu_r = \nu_{r0} + \nu_{\text{CME}}(t, \xi) \\ \rho = \rho_0 + \rho_{\text{CME}}(t, \xi) \\ T = T_0 + T_{\text{CME}}(t, \xi). \end{cases} \quad (15)$$

where ν_{r0} , ρ_0 , and T_0 are the background values of the radial velocity, density, and temperature.

[35] In our simulation of the January 1997 event, we use the following values: perturbation ramp duration $\tau_1 = \tau_2 =$

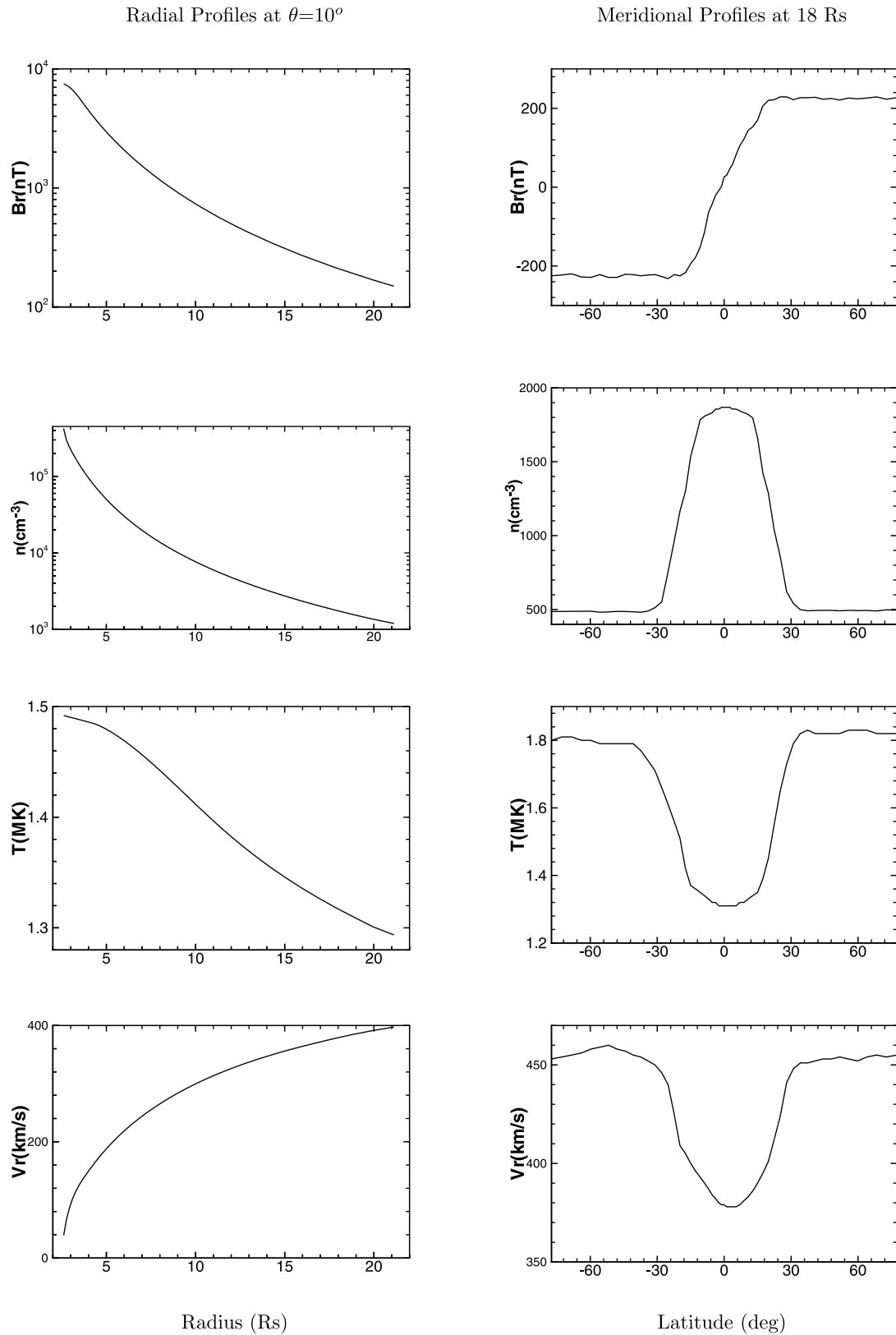


Figure 5. Ambient state of region I at 80 hours. Profiles of the radial magnetic field, proton number density, temperature, and the radial velocity at $\theta = 10^\circ$ and $\varphi = 180^\circ$ (radial profiles) are shown in the left column. The right hand column shows the same parameters at $r = 18 R_s$ and $\varphi = 180^\circ$ (meridional profiles).

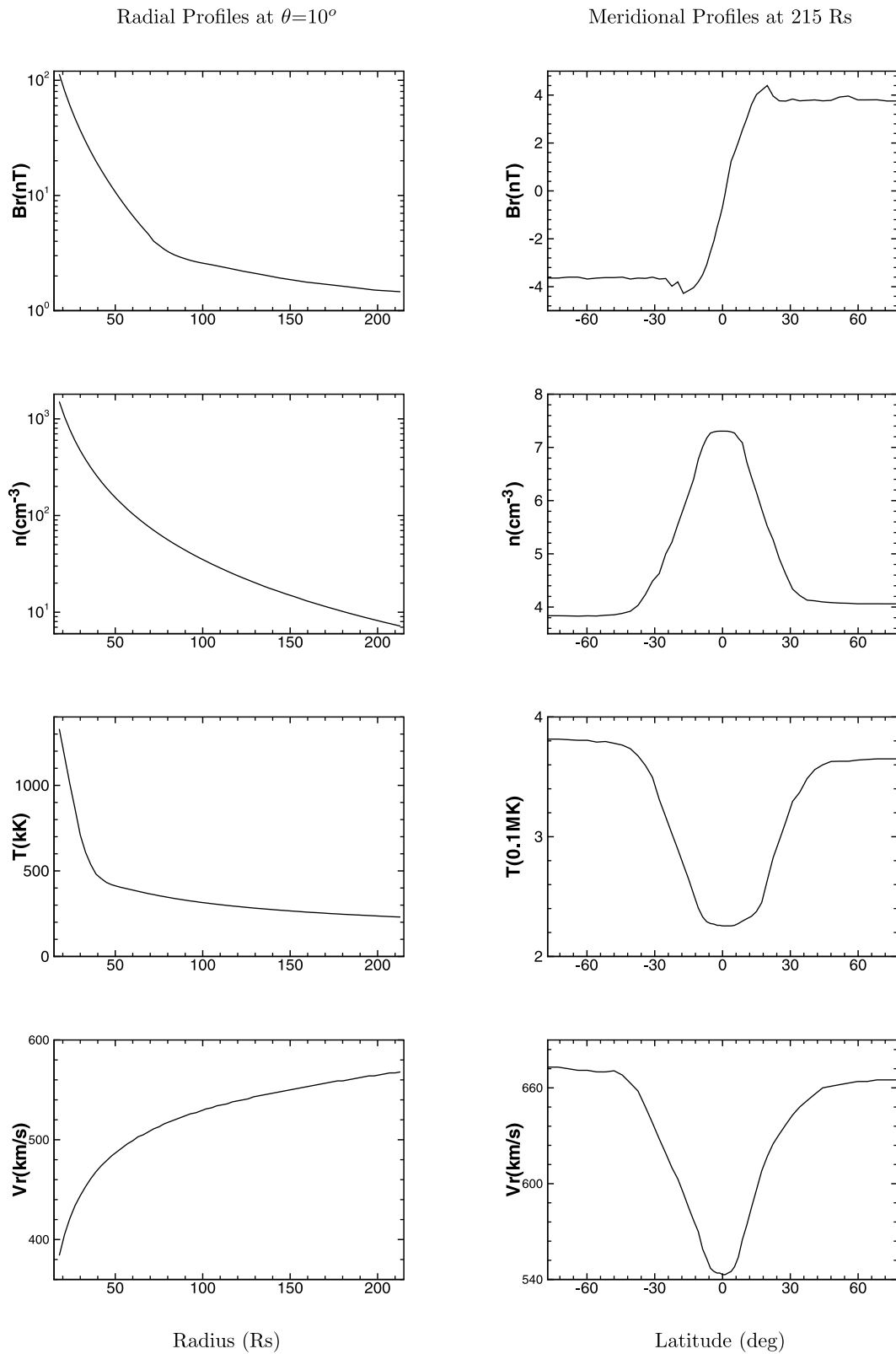


Figure 6. Ambient state of region II at 80 hours. Profiles of the radial magnetic field, proton number density, temperature, and the radial velocity at $\theta = 10^\circ$ and $\varphi = 180^\circ$ (radial profiles) are shown in the left column. The right hand column shows the same parameters at $r = 215 R_s$ and $\varphi = 180^\circ$ (meridional profiles).

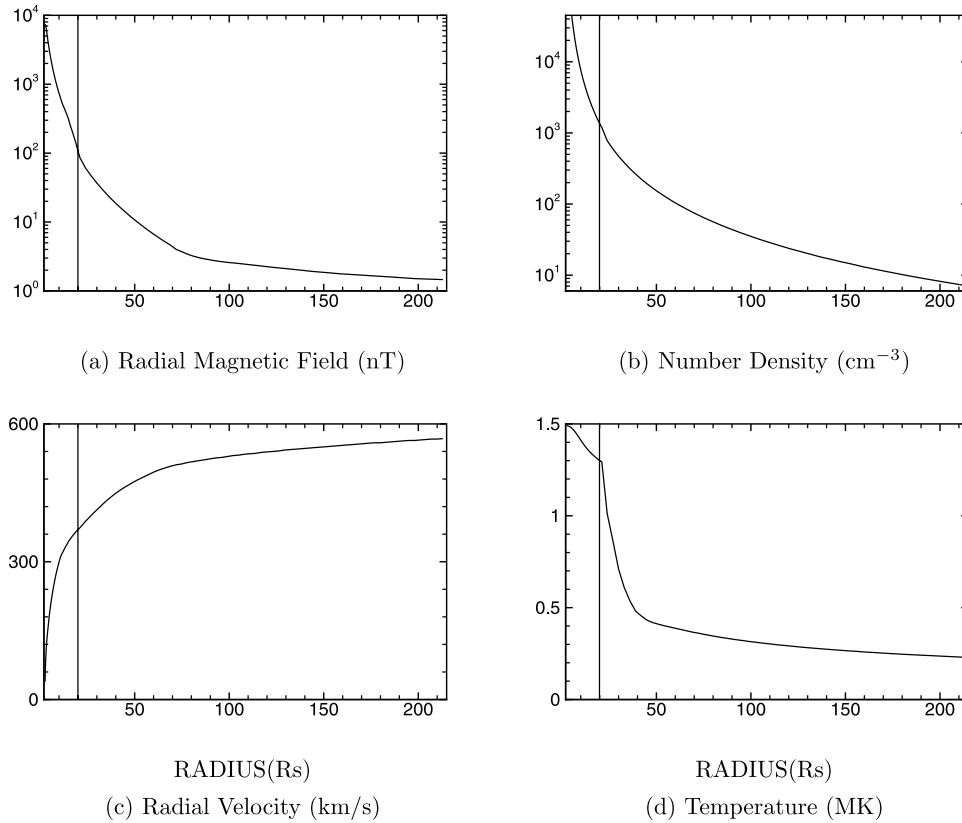


Figure 7. Plasma parameters in the corona (region I) with merging to the heliosphere (region II) at $\theta = 10^\circ$ and $\varphi = 180^\circ$ as a function of heliocentric distance for the ambient state at 80 hours. The interface between coronal and heliospheric models (at 22 Rs) is identified by the vertical black line.

0.5 hour; the perturbation duration at maximum value $\tau_m = 1$ hour and maximum values of the radial velocity, density, and temperature are $V_{\max} = 160$ km/s, $\rho_{\max} = 9 \times 10^7$ cm $^{-3}$, $T_{\max} = 1.5 \times 10^6$ K.

5. Results and Discussion

[36] Figures 8a and 8b show the positions of CME fronts at $\varphi = 180^\circ$ and at $\theta = 0^\circ$, $\theta = 20^\circ$, and $\theta = 45^\circ$ in the corona and heliosphere. From this figure we can clearly see the evolution of the CME propagation at three different latitudes of the Northern Hemisphere. In particular, they show that, at the equator or almost along the current sheet, the CME propagates faster at the equator than at other locations. This behavior is consistent with the observational result that the transient disturbances caused by solar activities would deflect toward the heliospheric current sheet as they travel to the Earth [Wei and Dryer, 1991; Feng and Zhao, 2006]. During the period of this event, the heliospheric current sheet lies almost on the solar equator. Note that the characteristics of the CME propagation show nonuniform acceleration and deceleration.

[37] The relative density $((\rho - \rho_0)/\rho_0)$, where ρ is the total density and ρ_0 the density of the background wind, is shown in Figure 9 at six consecutive times (pairs of plots, Figures 9a–9f). Each pair shows the projection in the meridional plane (left panel) and equatorial plane (right panel). The radial scales on Figures 9 and 9b are from 2.5 to 22 Rs and from 2.5 to 215 Rs in Figures 9c to 9f. The

meridional directions are $\varphi = 180^\circ$ in the left panels of Figures 9a, 9b, and 9c, $\varphi = 150^\circ$ in left panel of Figure 9d, and $\varphi = 135^\circ$ in the left panels of Figures 9e and 9f.

[38] Figure 10 shows the evolution of the velocity-distance profile in the direction $\theta = 0^\circ$ and the meridional directions selected for each panel in Figure 9. Figures 9a–9f and 10a–10f separately show the CME interaction with the background solar wind flow at 2 hours, 5 hours, 20 hours, 40 hours, 60 hours, and 80 hours after its launch from the inner boundary of 2.5 Rs. Note that the density maxima of Figure 9 and the slope changes in all trajectories of Figure 10 are consistent with the location of the ICME’s shock front in Figure 8. Note also that the sharp shock (Figure 9a) decays rapidly with both time and heliographic longitudinal position.

[39] Note that the CME was centered at $\theta = -20^\circ$, $\varphi = 183^\circ$. We notice from Figure 9, that the initially elliptical ejecta becomes circular and then develops into a “pancake” structure both in the meridional plane and equatorial plane. This structural development is a consequence of the combined effects of (1) kinematic expansion, as the ejecta moves into an ever larger spherical volume, (2) dynamic evolution, as the ejecta plows into slower ambient solar wind ahead, and (3) radial flow collision, lateral material expansion, and interactions with the background velocity and density structures [Odstreil et al., 1996a, 1996b; Odstreil and Pizzo, 1999; Dryer et al., 2001, 2004; Riley et al., 2004].

[40] From Figure 10, we can see how ICME propagation influences the bulk velocity. At 2 hours, influenced by the CME which was introduced near the inner boundary of

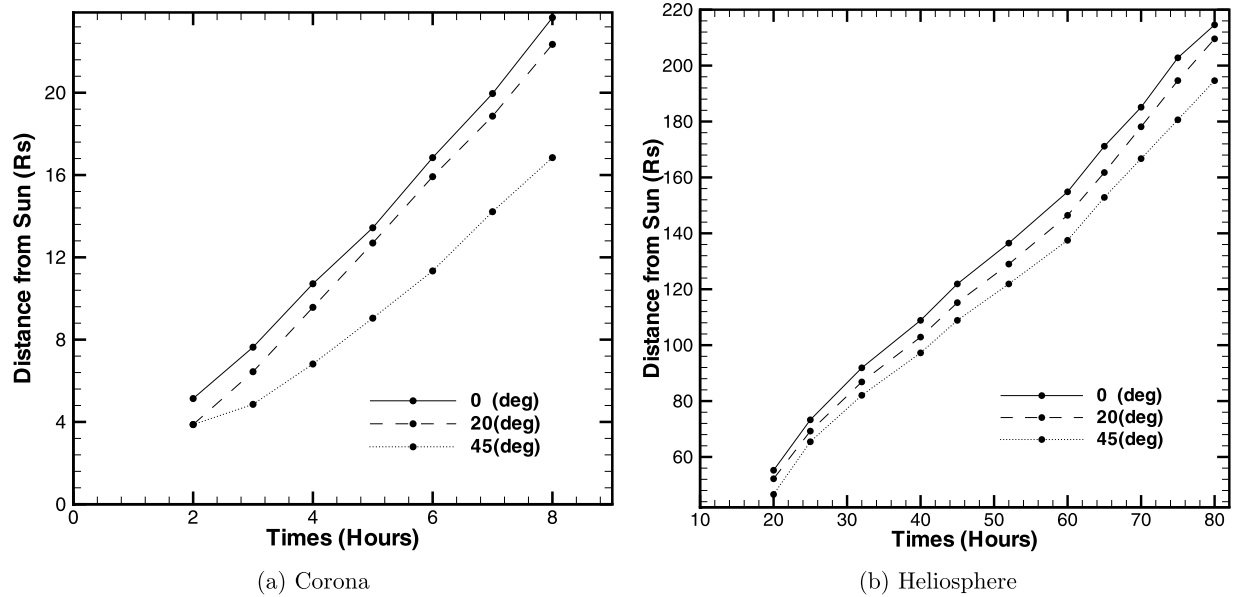


Figure 8. Evolution of the position of CME front in the corona (1–20 Rs) and heliosphere (20–215 Rs) at $\theta = 0^\circ$ (equator, solid lines), $\theta = 20^\circ$ (dashed lines), and $\theta = 45^\circ$ (dotted lines), respectively, for $\varphi = 180^\circ$.

2.5 Rs as a time-dependent pulse, the plasma velocity at ~ 6 Rs sharply increased to ~ 500 km/s, which is significantly greater than the background solar wind speed at this location (see Figure 5). After 5 hours, when the ICME has reached ~ 17 Rs, the bulk speed is ~ 550 km/s, while the radial background solar wind speed at this location is ~ 380 km/s. Gradually, through these interactions, the bulk velocity will finally return to its background speed of ~ 550 km/s shown in Figures 10a and 10b. At 20, 40, 60, and 80 hours, as the solar wind speed increases while the influence of the ICME decays, the slope changes in these curves from Figures 10c to 10f become less sharp. We can still find the peak of the ICME, within our computational domain, in these three panels, ~ 50 , ~ 90 , and ~ 130 Rs at 20, 40, and 60 hours, respectively; the ICME location is much more clearly seen in the density plots of Figure 9. At 80 hours, the CME front has propagated out beyond the Earth’s orbit, and the bulk velocity increases to ~ 640 km/s at this location.

[41] Figure 11 shows the comparison of the computed plasma and field parameters at 215 Rs in Figure 11b with the observed magnetic cloud of January 1997 shown in Figure 11a. This figure clearly indicates a qualitative resemblance (magnetic field maximum of $|B|$, B_x , B_y , B_z , field rotation, low temperature, and increasing $|B|$, B_x , B_y , B_z , density, velocity). One of the reasons why quantitative agreement is not expected is that the present model, like many others already mentioned, is only a single-fluid model. More importantly, there exist other two extremely important and still unsolved reasons as pointed out by Dryer [1998] and now recognized by many other modelers [Fry *et al.*, 2001; Odstroil *et al.*, 2004a, 2004b]. These two reasons are as follows: (1) uncertainty of the initial realistic solar wind and IMF background conditions and (2) uncertainty of the appropriate solar observations to use for “mimicking” solar flare filament and CME initiation input pulse conditions. In the ambient pre-CME state, the simu-

lated velocity is ~ 550 km/s shown in Figures 7c and 10 and, at the ICME maximum, it is ~ 650 km/s shown in Figure 11. In fact, these values are a little higher than the observation. The reason for this may be from our volumetric heating. The heating process is unclear up to now. The choice of such heating may give some favorable results but not all. It is usually believed [Wu *et al.*, 2006] that IP shock travels faster in fast solar wind, which may be another plausible reason for our high-speed ICME. To some extent, our establishment of using more observational data such as magnetic fields and the density by constraining the model is to try to avoid the uncertainty of the initial realistic solar wind. But, the approximate solar observations to use for “mimicking” solar flare/filament and CME imitation are challenging problems. It can be believed that more solar and interplanetary observations will clarify these uncertainties.

[42] By examining the computed total, x coordinate, y coordinate, z coordinate magnetic field profile, density profile, temperature profile, and velocity profile results given in Figure 11b we notice that the fast-mode shock arrived at 1 AU and ~ 82 hours after the initiation of the CME, since we use 17:34 UT on 6 January 1997 as the onset time (vertical dotted line in Figure 11a) (see section 2). These computed results are quite in accord with the interplanetary shock observed by the WIND spacecraft located in the solar wind upstream of Earth at 01:04 UT on 10 January 1997 (vertical dashed line in Figure 11a) and also with the magnetic cloud that passed the WIND spacecraft at 04:00 UT on 10 January 1997 (vertical solid line in Figure 11a) [Cane and Richardson, 2003]. We believe that the lack of a sharp shock jump in the simulated physical parameters is a consequence of the two reasons mentioned above. From the computed B_z field shown in Figure 11b, we find that the field turns southward at ~ 69 hours and then northward at ~ 78 hours. This magnetic field south-north rotations are mainly due to passing through the helical field

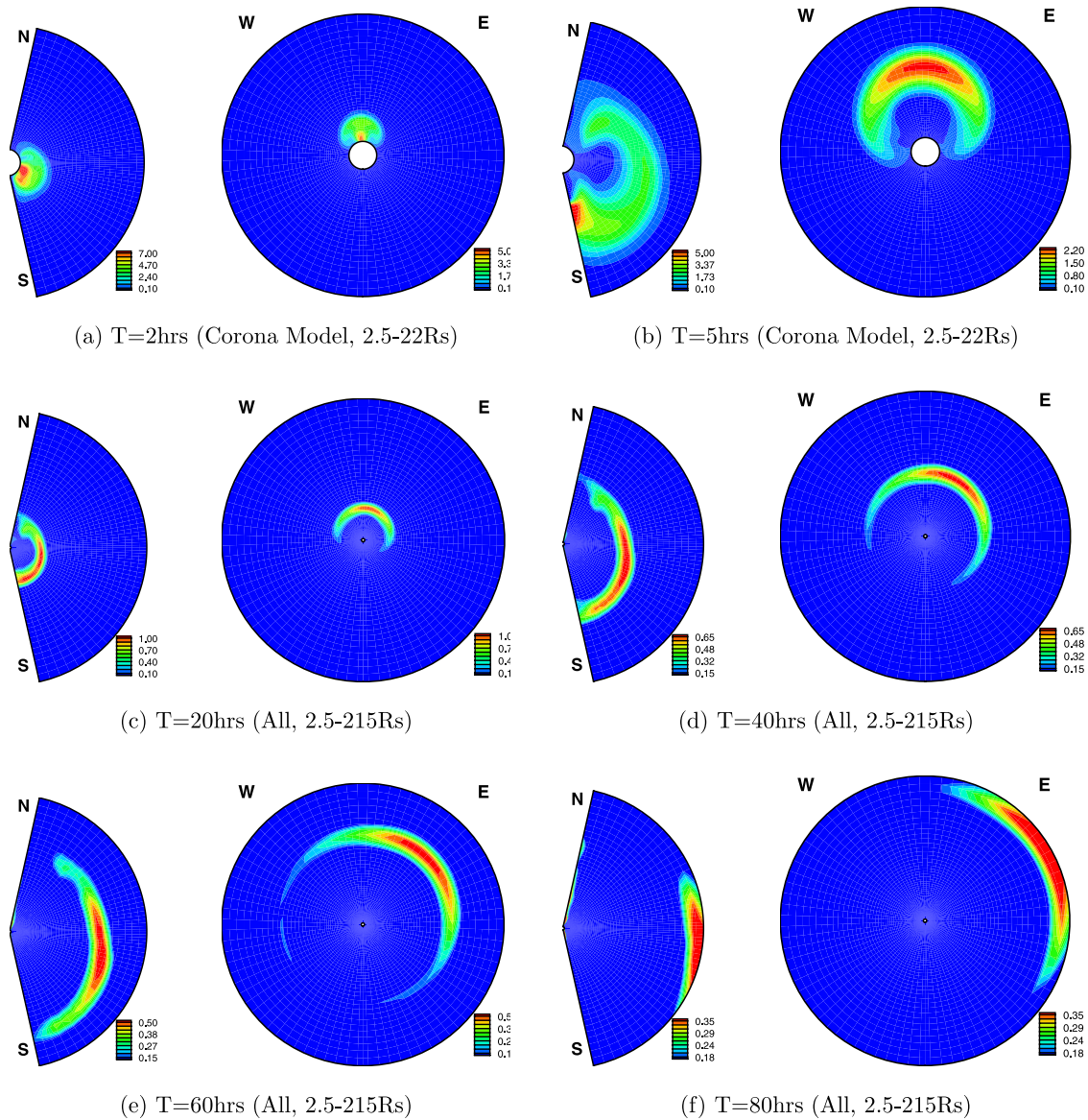


Figure 9. Evolution of the density contours $((\rho - \rho_0)/(\rho_0))$ at six consecutive times (pairs of plots, Figures 9a–9f). Each pair shows the projection in the meridional plane (left panel) and equatorial plane (right panel). Figures 9a and 9b are from 2.5 to 22 Rs at, respectively, $t = 2$ hours and at $t = 5$ hours in region I (coronal model). Figures 9c to 9f are from 2.5 to 215 Rs in both regions I and II at, respectively, $t = 20, 40, 60,$ and 80 hours. The meridional planes are as follows: $\varphi = 180^\circ$ in the left panels of Figures 9a, 9b, and 9c; $\varphi = 150^\circ$ in the left panel (Figure 9d), and $\varphi = 135^\circ$ in the left panels of Figures 9e and 9f. Note how the ambient high density (Figure 2) south and east of the Earth dominates the ICME’s response in those directions. Earth is at the top of each equatorial panel.

of the CME mentioned by *Wu et al.* [1999]. By examining simultaneously the computed density, temperature, and velocity profiles shown in Figure 11b, we can see that the largest density enhancement (in the first part of day 11) can be identified with the plasma compressed in the helmet dome and the additional plasma swept up by the system in the undisturbed corona during the initial CME propagation. This plasma is hot, as seen in the temperature profile (Figure 11b), because this represents the shocked, compressed plasma. These results are also in agreement with those of the asymmetric (2.5D) MHD model given by *Wu et al.* [1999]. We again stress again that our one-fluid (proton)

model can not account for the high temperature in a magnetic cloud and the anticorrelation between the electron temperature and density. The fact that our results (neglecting an initial flux rope configuration at the Sun) appear to be in accord with some of the results given by *Wu et al.* [1999], who used an initial flux rope to simulate CME initiation processes due to the filament eruption for this 6–11 January 1997 simulation exercise. The difference and similarity between the present study and the work of *Wu et al.* [1999] require further investigation. For example, it is possible that the IMF can move in a variety of ways behind a shock wave as demonstrated in two dimensions

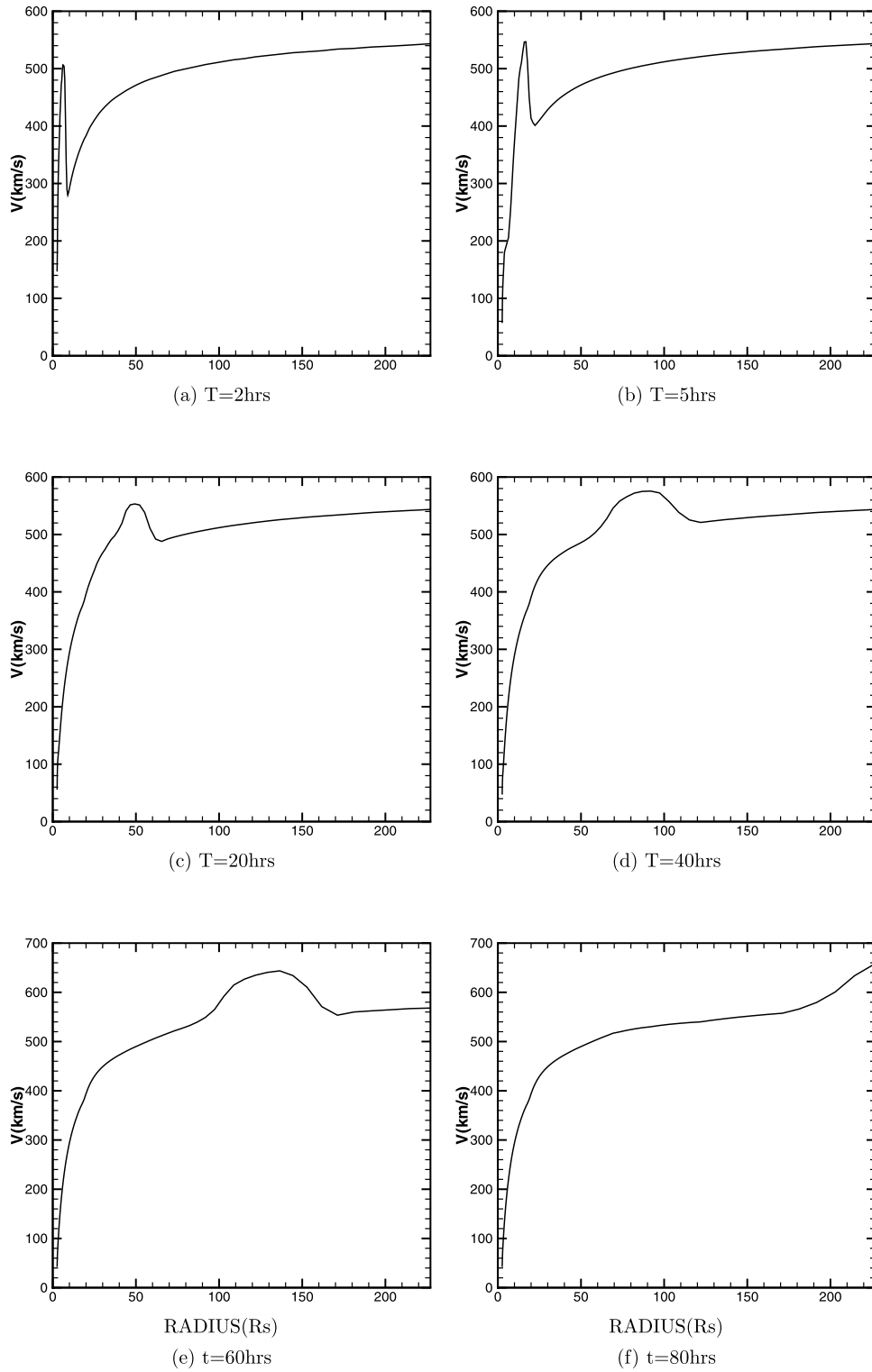


Figure 10. (a, b, and c) Evolution of the bulk velocity versus heliocentric distance from 2.5 to 215 R_s along the lines of $\theta = 0^\circ$ and $\varphi = 180^\circ$, (d) $\varphi = 150^\circ$, (e and f) and $\varphi = 135^\circ$.

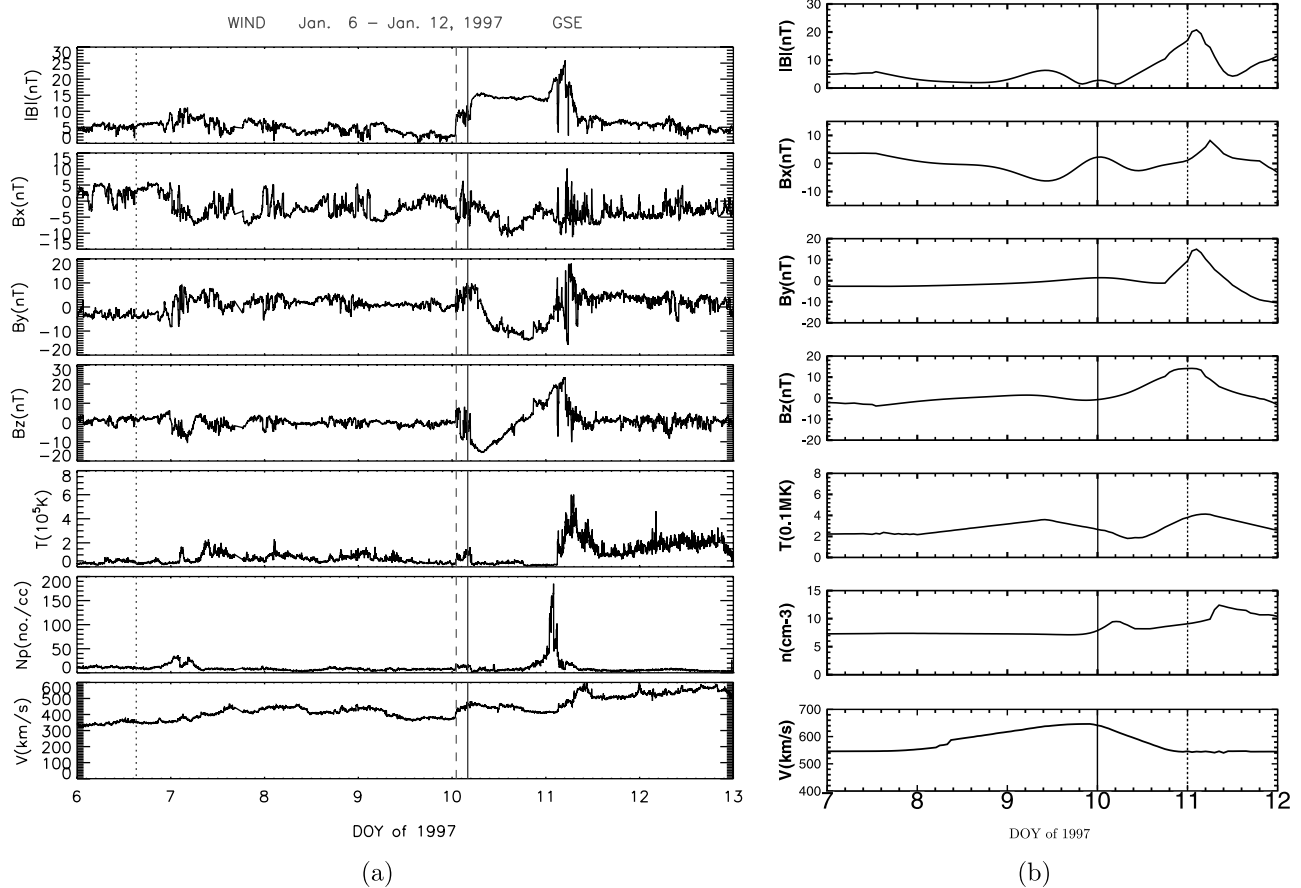


Figure 11. (a) Measured (WIND spacecraft) magnetic field and solar wind parameters from 6–13 January 1997 are as follows (top to bottom): the magnetic field strength $|B|$, B_x , B_y , B_z , the proton temperature T , the proton density N_p , and the magnitude of the bulk velocity V . The vertical short dashed line denotes the flare time (see section 2). The vertical long dashed line shows the time of the actual ICME’s shock arrival at WIND. The vertical solid line is the estimated (Cane and Richardson, 2003) ICME’s arrival time. (b) MHD simulation of magnetic field and plasma parameters corresponds to the measurement at 1 AU from 6–11 January 1997 as follows (top to bottom): the magnetic field strength $|B|$, B_x , B_y , B_z , the plasma temperature T , the number density n , and the magnitude of the bulk velocity V . The vertical solid line and short dashed line, respectively, correspond to DOY 10 and 11.

by Dryer *et al.* [1984, p. 205], via the classical circular IMF hodogram, and in three dimensions by Wu *et al.* [1996]. One must, therefore, question the need for extensive considerations of flux ropes as a major part of most ICMEs. In fact, it has been demonstrated [Richardson and Cane, 2005] that only 15% of all ICMEs intercepted at Earth have the features of a flux rope (magnetic cloud).

6. Conclusion

[43] We have used a three-dimensional time-dependent, numerical MHD model based on a code by Feng *et al.* [2005] to investigate large-scale background solar wind structures and the propagation of a specific ICME and its shock wave in a nonuniform background solar wind flow derived from observed magnetic field and density at the source surface.

[44] To establish the self-consistent structures on the source surface of 2.5 Rs for background solar wind, we have used the observational data of the solar magnetic field, K-coronal brightness (density) (Figure 2), and the first principle of MHD. By using the self-consistent source

surface structures as initial and boundary conditions, we have successfully developed a three-dimensional MHD regional combination numerical model of the background solar wind whose domain extends from source surface of 2.5 Rs to near the Earth’s orbit (215 Rs) with consideration of solar rotation and volumetric heating. The three-dimensional MHD equations are solved by combining a time relaxation numerical technique in the corona with a marching-along-radius method in the heliosphere as used by Feng *et al.* [2005]. The ratio of specific heats is given as $\gamma = 1.05$ at the coronal model and $\gamma = 1.2$ at the heliospheric model. Our numerical results of background solar wind (Figures 3, 4, 5, 6, and 7) show that (1) we have reproduced a typical Archimedes’ spiral lines of magnetic field topology in the equatorial plane by including the solar rotation, (2) the configurations of both corona and heliosphere consist of a dense and slow flow near the current sheet (the range of latitude is about $\pm 25^\circ$), as well as high-speed wind in high latitude, and (3) the absolute value of the radial magnetic field remains almost constant outside of the current sheet, independent of latitude, which is consistent with Ulysses observations.

[45] We then investigated the dynamical interaction of a CME with the background solar wind flow between 2.5 and 215 Rs. The CME is introduced at the inner boundary of 2.5 Rs as a time-dependent pulse to mimic the effects of a filament eruption. We chose the well-defined halo-CME event of 6–12 January 1997 for our first test because of all the data available from the SOHO/LASCO and WIND spacecraft. The numerical results of the CME propagation are shown in Figures 8, 9 and 10. The density peaks of Figure 9 and the slope changes in all curves of Figure 10 are consistent with the location of the CME front in Figure 8. Figures 8, 9, and 10 also show that, (1) at the equator, the CME propagates faster than that at other location, (2) the initially elliptical ejecta becomes circular and then develops into a “pancake” structure, (3) the CME propagation is influenced by the bulk velocity.

[46] When the ejecta reached 1 AU, its physical parameters (Figure 11) resembled qualitatively the observations of the magnetic cloud recorded by the WIND spacecraft [Burlaga et al., 1998]. This demonstrates that a CME, initiated by CME model, may evolve into an interplanetary ejecta or magnetic cloud. However, the fact that our model did not incorporate a modeled flux rope configuration (as was done by Wu et al. [1999]) suggests, as discussed above, that it may not be necessary to use such assumptions in three-dimensional MHD simulations to explain the flux rope-type hodogram discussed by Burlaga et al. [1998, and references therein]. In front of the ejecta, the density enhancement exhibited the characteristics of the observed CME to some degree; however, further studies should consider other forms of the input pulse to mimic the CME as well as the form of nonuniform background solar wind in three dimensions.

[47] In summary, in this study, we find that this three-dimensional MHD model, with the self-consistent structures on the source surface as input, provides a relatively satisfactory comparison with the observations. While this model still needs improvement, there exist many other factors that should be studied, such as, heating and acceleration mechanism of solar wind and better understanding of CME initiation.

[48] **Acknowledgments.** This work is jointly supported by National Natural Science Foundation of China (40621003, 40504020, 40536029, and 40523006), 973 Program under grant 2006CB806304, and the CAS International Partnership Program for Creative Research Teams. Dr. S. T. Wu is supported by NASA via grant NAG5-2843 to UAH and grant NNG04GD59G via subcontract to UAH from AAMU, and NSF via grant ATM 0316115. We appreciate the valuable suggestions and comments given to us by the referees.

[49] Zuyin Pu thanks the reviewers for their assistance in evaluating this paper.

References

Asai, K., M. Kojima, A. Yokobe, et al. (1998), Heliospheric tomography using interplanetary scintillation observations: 3. Correlation between speed and electron density fluctuations in the solar wind, *J. Geophys. Res.*, *103*, 1991–2001.

Burlaga, L. F., et al. (1998), A magnetic cloud containing prominence material: January 1997, *J. Geophys. Res.*, *103*, 227.

Cane, H. V., and I. G. Richardson (2003), Interplanetary coronal mass ejections in the near-Earth solar wind during 1996–2002, *J. Geophys. Res.*, *108*(A4), 1156, doi:10.1029/2002JA009817.

Detman, T. R., Z. Smith, M. Dryer, C. D. Fry, C. N. Arge, and V. J. Pizzo (2006), A hybrid heliospheric modeling system: I. Background solar wind, *J. Geophys. Res.*, *111*, A07102, doi:10.1029/2005JA011430.

Dryer, M. (1974), Interplanetary shock waves generated by solar flares, *Space Sci. Rev.*, *15*, 403–468.

Dryer, M. (1975), Interplanetary shock waves: Recent developments, *Space Sci. Rev.*, *17*, 277–325.

Dryer, M. (1982), Coronal transient phenomena, *Space Sci. Rev.*, *33*, 233–275.

Dryer, M. (1994), Interplanetary studies: Propagation of disturbances between the Sun and the magnetosphere, *Space Sci. Rev.*, *6*(3/4), 363–419.

Dryer, M. (1998), Multi-dimensional MHD simulation of solar-generated disturbances: Space weather forecasting of geomagnetic storms, *AIAA J.*, *36*(3), 365–370.

Dryer, M., S. T. Wu, G. Gislason, S. M. Han, Z. K. Smith, J. F. Wang, D. F. Smart, and M. A. Shea (1984), Magnetohydrodynamic modeling of interplanetary disturbances between the Sun and Earth, *Astrophys. Space Sci.*, *105*, 187–208.

Dryer, M., C. D. Fry, W. Sun, C. S. Deehr, Z. Smith, S.-I. Akasofu, and M. D. Andrews (2001), Prediction in real-time of the 2000 July 14 heliospheric shock wave and its companions during the “Bastille” epoch, *Sol. Phys.*, *204*, 267–286.

Dryer, M., C. D. Fry, W. Sun, C. S. Deehr, and S.-I. Akasofu (2004), Real-time predictions of interplanetary shock arrivals at L1 during the “hal-loeewen 2003” epoch, *Space Weather*, *2*, S09001, doi:10.1029/2004SW000087.

Feng, X., and X. Zhao (2006), Geoeffective analysis of CMEs under current sheet magnetic coordinates, *Astrophys. Space Sci.*, doi:10.1007/s10509-006-9039-6.

Feng, X., et al. (2003a), A Class of two-step TVD MacCormack type numerical scheme for MHD equations, *Chin. J. Space Sci.*, *23*, 401–412.

Feng, X., S. T. Wu, F. Wei, and Q. Fan (2003b), A class of TVD type combined numerical scheme for MHD equations with a survey about numerical methods in solar wind simulations, *Space Sci. Rev.*, *107*, 43–53.

Feng, X., et al. (2005), A comparative study on 3-D solar wind structure observed by Ulysses and MHD simulation, *Chin. Sci. Bull.*, *50*(7), 672–678.

Fox, N. J., M. Peredo, and B. J. Thompson (1998), Cradle-to-grave tracking of January 6–11, 1997, Sun–Earth connection event, *Geophys. Res. Lett.*, *25*, 2461.

Fry, C. D., W. Sun, C. S. Deehr, M. Dryer, Z. Smith, S.-I. Akasofu, M. Tokumaru, and M. Kojima (2001), Improvements to the HAF solar wind model for space weather predictions, *J. Geophys. Res.*, *106*, 20,985–21,001.

Fry, C. D., M. Dryer, C. S. Deehr, W. Sun, S.-I. Akasofu, and Z. Smith (2003), Forecasting solar wind structures and shock arrival times using an ensemble of models, *J. Geophys. Res.*, *108*(A2), 1070, doi:10.1029/2002JA009474.

Fry, C. D., M. Dryer, W. Sun, C. S. Deehr, Z. Smith, A. Aran, D. Lario, B. Sanahuja, T. R. Detman, and S.-I. Akasofu (2005), Key links in space weather forecasting solar-generated shocks and proton acceleration, *AIAA J.*, *43*(5), 987–993.

Gosling, J. T. (1990), Coronal mass ejections and magnetic flux ropes in interplanetary space, in *Physics of Magnetic Flux Ropes*, *Geophys. Monogr. Ser.*, *58*, edited by C. J. Russell, E. R. Priest, and L. C. Lee, pp. 343–364, AGU, Washington, D. C.

Groth, C. P. T., D. L. D. Zeeuw, T. I. Gombosi, and K. G. Powell (2000), Global three-dimensional MHD simulation of a space weather event: CME formation, interplanetary propagation, and interaction with the magnetosphere, *J. Geophys. Res.*, *105*(A11), 25,053–25,078.

Han, S. M., S. T. Wu, and M. Dryer (1988), A three-dimensional time-dependent numerical method of supersonic, super-Alfvénic MHD flow, *Comput. Fluids*, *16*, 81–103.

Hoeksema, J. T. (1992), Evolution of the solar and coronal field structure: 1976–1991, *Proc. First SOLTIP Symp.*, edited by S. Fischer and M. Vandas, Astron. Inst. of the Czech. Acad. of Sci., Prague, Czechoslovakia, *1*, pp. 119–228.

Hundhausen, A. J., J. T. Burckepile, and O. C. St. Cyr (1994), Speeds of coronal mass ejections: SMM observations from 1980 and 1984–1989, *J. Geophys. Res.*, *99*(A4), 6,543–6,552.

Jackson, B. V., P. L. Hick, M. Kojima, et al. (1998), Heliospheric tomography using interplanetary scintillation observations: 1. Combined Nagoya and Cambridge data, *J. Geophys. Res.*, *103*(A6), 12,049–12,067.

Janardhan, P., V. Balasubramanian, S. Ananthkrishnan, M. Dryer, A. Bhatnagar, and P. S. McIntosh (1996), Traveling interplanetary disturbances detected using interplanetary scintillation at 327 MHz, *Sol. Phys.*, *166*, 379–401.

Kojima, M., K. Fujiki, T. Ohmi, M. Tokumaru, A. Yokobe, and K. Hakamada (2001), Latitudinal velocity structures up to the solar poles estimated from interplanetary scintillation tomography analysis, *J. Geophys. Res.*, *106*(A8), 15,677–15,686.

- Liewer, P. C., J. R. Hall, M. De Jong, D. G. Socker, R. A. Howard, P. C. Crane, P. Reiser, N. Rich, and A. Vourlidas (2001), Determination of three-dimensional structure of coronal streamers and relationship to the solar magnetic field, *J. Geophys. Res.*, *106*(A8), 15,903–15,915.
- Linker, J., A. Mikic, Z. Bisecker, et al. (1999), Magnetohydrodynamic modeling of the solar corona during whole Sun month, *J. Geophys. Res.*, *104*(A5), 9809–9830.
- Manchester, W. B., IV, T. I. Gombosi, D. L. DeZeeuw, I. V. Sokolov, I. I. Roussev, K. G. Powell, J. Kóta, G. Tóth, and T. H. Zurbuchen (2005), Coronal Mass Ejection shock and sheath structures relevant to particle acceleration, *Astrophys. J.*, *622*, 1225–1239.
- Manoharan, P. K., S. Ananthakrishnan, M. Dryer, T. R. Detman, H. Leinbach, M. Kojima, T. Watanabe, and J. Khan (1995), Solar wind velocity and normalized scintillation index from single station IPS observations, *Sol. Phys.*, *156*(2), 377–393.
- McKenna-Lawlor, S., M. Dryer, M. D. Kartalev, Z. Smith, C. D. Fry, W. Sun, C. S. Deehr, K. Kecskemeti, and K. Kudela (2006), Near real-time predictions of the arrival at the earth of flare-generated shocks during solar cycle 23, *J. Geophys. Res.*, *111*, A11103, doi:10.1029/2005JA011162.
- Michalek, G., N. Gopalswamy, and S. Yashiro (2003), A new method for estimating widths, velocities and source location of halo coronal mass ejections, *Astrophys. J.*, *584*, 472–478.
- Odstreil, D., and V. J. Pizzo (1999), Three-dimensional propagation of coronal mass ejections (CMEs) in a structured solar wind flow: 1. CME launched within the streamer belt, *J. Geophys. Res.*, *104*(A1), 483–492.
- Odstreil, D., M. Dryer, and Z. Smith (1996a), Interaction of an interplanetary shock with the heliospheric plasma sheet, *Proc. Solar Wind 8 Symposium*, Dana Point, CA, 26–30 June 1995, Amer. Inst. Physics, Woodbury, NY, pp. 457–460.
- Odstreil, D., M. Dryer, and Z. Smith (1996b), Propagation of an interplanetary shock along the heliospheric plasma sheet, *J. Geophys. Res.*, *101*(A9), 19,973–19,986.
- Odstreil, D., J. A. Linker, R. Lionello, Z. Mikic, P. Riley, V. J. Pizzo, and J. G. Luhmann (2002a), Merging of coronal and heliospheric numerical 2-D MHD models, *J. Geophys. Res.*, *107*(A12), 1493, doi:10.1029/2002JA009334.
- Odstreil, D., J. A. Linker, R. Lionello, Z. Mikic, P. Riley, V. J. Pizzo, and J. G. Luhmann (2002b), 3-D MHD simulations of CMEs by coupled coronal and heliospheric models, In: *Proceeding of the 10th European Solar Physics Meeting*, ESA SP-506, 95–98.
- Odstreil, D., V. J. Pizzo, J. A. Linker, P. Riley, R. Lionello, and Z. Mikic (2004a), Initial coupling of coronal and heliospheric numerical magnetohydrodynamic codes, *J. Atmos. Sol. Terr. Phys.*, *66*, 1311–1320, doi:10.1016/j.jastp.2004.04.007.
- Odstreil, D., P. Riley, and X. P. Zhao (2004b), Numerical simulation of the 12 May 1997 interplanetary CME event, *J. Geophys. Res.*, *109*, A02116, doi:10.1029/2004JA010745.
- Odstreil, D., V. J. Pizzo, and C. N. Arge (2005), Propagation of the 12 May 1997 interplanetary coronal mass ejection in an evolving solar wind structures, *J. Geophys. Res.*, *110*, A02106, doi:10.1029/2003JA010135.
- Parker, E. N. (1963), *Interplanetary Dynamical Processes*, Wiley-Interscience, Hoboken, N. J.
- Pizzo, V. (1982), A three-dimensional model of corotating streams in the solar wind: 3. Magnetohydrodynamic streams, *J. Geophys. Res.*, *87*(A6), 4374–4394.
- Plunkett, S. P., et al. (1997), The relationship of green-line transients to white-light coronal mass ejections, *Sol. Phys.*, *175*, 699.
- Richardson, I. G., and H. V. Cane (2005), A survey of interplanetary coronal mass ejections in the near-Earth solar wind during 1996–2005, in *Proceedings of Solar Wind 11-SOHO, 'Connecting Sun with Heliosphere'*, Whistler, B.C., Canada, June 13–17, 2005, ESA Publ. SP-592, 755–758.
- Rickett, B. T., and W. A. Coles (1991), Evolution of the solar wind structure over a solar cycle: Interplanetary scintillation velocity measurements compared with coronal observations, *J. Geophys. Res.*, *96*(2), 1717–1735.
- Riley, P., J. T. Gosling, and V. J. Pizzo (1997), A two-dimensional simulation of the radial and latitudinal evolution of a solar wind disturbance driven by a fast, high-pressure coronal mass ejection, *J. Geophys. Res.*, *102*(A7), 14,677–14,686.
- Riley, P., J. A. Linker, and Z. Mikic (2001), An empirically driven global MHD model of the solar corona and inner heliosphere, *J. Geophys. Res.*, *106*(A8), 15,889–15,901.
- Riley, P., J. A. Linker, Z. Mikic, and D. Odstreil (2004), Magnetohydrodynamic modeling of interplanetary CMEs, *IEEE Trans. Plasma Sci.*, *32*(4), 1415–1424.
- Smith, E. J. (2001), The heliospheric current sheet, *J. Geophys. Res.*, *106*(A8), 15,819–15,831.
- Smith, Z., and M. Dryer (1990), MHD study of temporal and spatial evolution of simulated interplanetary shocks in the ecliptic plane within 1 AU, *Sol. Phys.*, *129*, 387–405.
- Suess, S. T., A.-H. Wang, and S. T. Wu (1996), Volumetric heating in coronal streamers, *J. Geophys. Res.*, *101*(A9), 19,957–19,966.
- Tóth, G. (2000), The $\nabla \cdot B = 0$ constraint in shock-capturing magnetohydrodynamics codes, *J. Comput. Phys.*, *161*, 605–652.
- Usmanov, A. V. (1993), A global numerical 3-D MHD model of the solar wind, *Sol. Phys.*, *146*, 377–396.
- Usmanov, A. V., and M. Dryer (1995), A global 3D simulation of interplanetary dynamics in June 1991, *Sol. Phys.*, *159*(2), 347–370.
- Usmanov, A. V., M. L. Goldstein, B. P. Besser, and J. M. Frizel (2000), A global MHD solar wind model with WKB Alfvén waves: Comparison with Ulysses data, *J. Geophys. Res.*, *105*(A6), 12,675–12,695.
- Wang, Y. M., and N. R. Sheeley Jr. (1990), Solar wind speed and coronal flux-tube expansion, *Astrophys. J.*, *355*, 726–732.
- Wang, A.-H., S. T. Wu, S. T. Suess, and G. Poletto (1998), Global model of the corona with heat and momentum addition, *J. Geophys. Res.*, *103*(A2), 1,913–1,922.
- Webb, D. F., et al. (1997), Large-scale structures and multiple neutral lines associated with coronal mass ejections, *J. Geophys. Res.*, *102*(A11), 24,161.
- Webb, D. F., E. Cliver, N. Gopalswamy, H. Hudson, and O. St. Cyr (1998), The solar origin of the January 1997 coronal mass ejection, magnetic cloud, and geomagnetic storm, *Geophys. Res. Lett.*, *25*(14), 2469.
- Wei, F., and M. Dryer (1991), Propagation of solar flare-associated interplanetary shock waves in the heliospheric meridional plane, *Sol. Phys.*, *132*, 373–394.
- Wei, F., X. Xueshang, C. Hongchang, and Z. Qingjun (2003), Global distribution of coronal mass outputs and its relation with solar magnetic field structures, *J. Geophys. Res.*, *108*(A6), 1238, doi:10.1029/2002JA009439.
- Wu, C.-C., M. Dryer, and S. T. Wu (1996), Three-dimensional MHD simulation of interplanetary magnetic field changes at 1 AU as a consequence of simulated solar flares, *Ann. Geophys.*, *14*, 383–399.
- Wu, S. T., W. P. Guo, and M. Dryer (1997), Dynamical evolution of a coronal streamer-flux rope system: II. A self-consistent non-planar magnetohydrodynamic solution, *Sol. Phys.*, *170*, 265–282.
- Wu, S. T., W. P. Guo, D. J. Michels, and L. F. Burlaga (1999), MHD description of the dynamical relationships between a flux rope, streamer, coronal mass ejection, and magnetic cloud: An analysis of the January 1997 Sun-Earth connection event, *J. Geophys. Res.*, *104*(A7), 14,789–14,801.
- Wu, Y. Q., Y. H. Tang, Y. Dai, and G. P. Wu (2002), The solar origin of the 6 January 1997 coronal mass ejection, *Sol. Phys.*, *207*, 159–171.
- Wu, C.-C., X. S. Feng, S. T. Wu, M. Dryer, and C. D. Fry (2006), Effects of the interaction and evolution of interplanetary shocks on “background” solar wind speeds, *J. Geophys. Res.*, *111*, A12104, doi:10.1029/2006JA011615.
- Xiang, C. Q., and X. S. Feng (2006), An observation-based model of solar wind background, *Chin. J. Space Sci.*, *26*(3), 161–166.
- Zhao, X. P., and J. T. Hoeksema (1996), Effect of coronal mass ejections of the structure of the heliospheric current sheet, *J. Geophys. Res.*, *101*(A3), 4825–4834.
- Zhao, X. P., S. P. Plunkett, and W. Liu (2002), Determination of geometrical and kinematical properties of halo coronal mass ejections using the cone model, *J. Geophys. Res.*, *107*(A8), 1223, doi:10.1029/2001JA009143.

X. Feng, F. Shen, and C. Xiang, SIGMA Weather Group, State Key Laboratory for Space Weather, Center for Space Science and Applied Research, Chinese Academy of Sciences, Beijing 100080, China. (xfeng@spaceweather.ac.cn)

S. T. Wu, Center for Space Plasma and Aeronomic Research, The University of Alabama in Huntsville, Huntsville, AL 35899, USA.